Research Square

Preprints are preliminary reports that have not undergone peer review.
They should not be considered conclusive, used to inform clinical practice,
or referenced by the media as validated information.

Multi-Objective Optimization of MAG Welding Parameters for Minimizing Distortion and Residual Stress in Industrial-Scale Heavy Machinery Assemblies

Shahriar Bakrani
Tampere University - Hervannan Campus: Tampereen yliopisto - Hervannan kampus
Di Wu
Tampere University - Hervannan Campus: Tampereen yliopisto - Hervannan kampus
Heikki Selkälä
Ponsse Oyj
Hossein Mokhtarian
hossein.mokhtarian@tuni.fi
Tampere University - Hervannan Campus: Tampereen yliopisto - Hervannan kampus
https://orcid.org/0000-0002-6818-9044
Eric Coatanéa
Tampere University - Hervannan Campus: Tampereen yliopisto - Hervannan kampus

Research Article

Keywords: Thermal distortion, Welding, Finite Element Method, FEM, Thermomechanical Modelling, Multi-Objective Optimization, Metal Active Gas, MAG

Posted Date: November 4th, 2026

DOI: https://doi.org/10.21203/rs.3.rs-10958589/v1

License: This work is licensed under a Creative Commons Attribution 4.0 International License.
Read Full License

Multi-Objective Optimization of MAG Welding Parameters for Minimizing Distortion and Residual Stress in Industrial-Scale Heavy Machinery Assemblies

Shahriar Bakrani Balani[a], Di Wu[a], Heikki Selkälä[b], Hossein Mokhtarian[a]*, Eric Coatanéa[a]

[a] Faculty of Engineering and Natural Science, Tampere University,
33720 Tampere, Finland
[b] Ponsse Oyj, Ponssentie 22, 74200 Vieremä, Finland

* Corresponding author email address: hossein.mokhtarian@tuni.fi

Abstract

Residual stress, thermal deformation and warpage are the most important engineering problems for the welding structures. This problem is more significant for large industrial-scale structures, where higher heat input is demanded and temperature gradient is more significant. Residual stress and thermal deformation after welding could lead to inconsistency of tolerances, and in cases lead to reduced mechanical strength and ultimately failure. Although it is impossible to reduce thermal distortion to zero, finding optimum welding parameters could highly reduce the thermal deformation during welding. However, due to the large scale of the structure, thermal deformation and stress prediction and parameter optimization are extremely time consuming to be implemented in real practice. In this paper, we have performed a Multi-Objective Optimization (MOO) on the welding parameters on a case study provided by Ponsse Oyj company in order to reduce thermal deformation and thermal warpage due to heat delivered to the structure during Metal Active Gas (MAG) welding process within an acceptable computational time. A thermomechanical elasto-plastic model is created using Finite Element Method (FEM) to determine thermal deformation and residual stress. Furthermore, L-ANN-GWO MOO algorithm, which adopts adaptive surrogate modeling strategy to reduce the number of FEA evaluations, is used to find the optimum welding parameters (starting angle, travel speed, voltage, and current) subject to the preliminary Welding Procedure Specification (pWPS). Based on MOO, three process parameter combinations were suggested which could lead to up to more than 30-40% reduction in thermal distortion and 20-30% reduction in residual stress. Our studies show the importance of selecting proper welding starting point. Performed modelling-optimization approach used in this paper could be used for other large structures where there is excessive delivered heat.

Keywords: Thermal distortion, Welding, Finite Element Method, FEM, Thermomechanical Modelling, Multi-Objective Optimization, Metal Active Gas, MAG

Abbreviations

Artificial neural networks (ANN)
Back Propagation Neural Network (BPNN)
grey relational degree analysis (GRA)
Finite Element Method (FEM)
Kreisselmeier and Steinhauser (KS)
LASSO-Artificial Neural Network-Grey Wolf Optimizer (L-ANN-GWO)
Metal Active Gas (MAG)
Multi-Objective Optimization (MOO)
Multi-Objective Genetic Algorithm (MOGA)
Non-dominated Sorting Genetic Algorithm-III (NSGA-III)
Number of Function Evaluations (NFE)
Preliminary Welding Procedure Specification (pWPS)

1. Introduction

Welding is one of the most widely employed manufacturing processes in the fabrication of heavy machinery, construction equipment, ship structures, pressure vessels, and large-scale industrial components. The process enables the permanent joining of metallic parts with high structural integrity and cost-effectiveness, making it indispensable in modern manufacturing industries. However, the localized heat input generated during welding introduces complex thermal cycles that significantly influence the dimensional accuracy and structural performance of welded assemblies. During the welding process, the material in the vicinity of the weld zone experiences rapid heating followed by non-uniform cooling. These temperature gradients produce localized thermal expansion and contraction, which subsequently generate residual stresses and permanent deformations within the structure [1]. As a result, how to reduce residual stress and permanent deformation becomes one of the critical matters in welding quality management.

To realize the residual stress and distortion reduction, the first task is to predict them before welding. Different numerical modelling approaches are used for residual stress and distortion prediction [2]. Finite Element Method (FEM) numerical modelling is one of the most conventional and reliable methods for determination of residual stress and distortion. FEM numerical simulation could be used for modelling thermal stress during welding for different geometries. As an example, Deng et al. used thermo-elasto-plastic modelling for determination of welding distortion in large structures [3]. Long et al. used FEM for modelling thermal stress and distortion of thin plates during welding [4]. These advanced computational models could also be used during design phase in order to understand the thermal stress mechanism and design the welding process and geometry accordingly. On the other hand, based on developed FEM models, post-weld distortion mitigation methods could be used [5]. Controlling cooling rate of the welding [6,7] and applying mechanical tensioning [8] are the most common mitigation methods for reducing distortion [6]. Therefore, in the first step a thermomechanical FEM model has been developed to predict thermal distortion and residual stress.

The next task is to find the optimal welding parameters, such as voltage, current, travel speed, etc., to minimize the residual stress and permanent deformation. To balance the different criteria and features and achieve good overall qualities, the welding parameter optimization becomes a Multi-Objective Optimization (MOO) problem. Different optimization approaches are applied to solve the multi-objective welding parameter optimization problem. One basic approach is to combine the multiple objectives into one single objective and solve it with single-objective optimization algorithms. For example, Karumuri et al. used grey relational degree analysis (GRA) approach to transform a MOO problem into a single-objective problem in optimizing a friction stir welding process [9]. To provide more solutions and improve the flexibility of the optimization, metaheuristic algorithms which can provide multiple optimal solutions (namely Pareto frontiers) were employed by other researchers in welding parameter optimization. A multi-objective genetic algorithm (MOGA) was used to reduce residual stress and distortion in an arc-welding process [10]. Non-dominated sorting genetic algorithm-III (NSGA-III) was employed to minimize the energy consumption and maximize the welding quality in a laser welding case study [11].

The main drawback of the metaheuristic algorithm is that it always needs many cost function evaluations to find the optimal results. When using FEM models as the cost function, the computational time of using such algorithms is usually too long to implement. For example, it is reported that one thermo-elasto-plastic simulation of a 600mm butt welding took more than 29 hours [12]. Considering the high number of cost function evaluation requirements of the metaheuristic algorithms (usually above 1000), it is impossible to perform welding parameter optimization fully using FEM models.

To solve this issue, surrogate models are utilized to approximate the time-consuming simulations and used as the cost functions in optimization. Artificial neural networks (ANN), or specifically the back propagation neural network (BPNN) are one of the popular surrogate models used to approximate the welding process [10,13,14]. Other popular surrogate models include response surface [15], random forest [16], convolutional neural network [17], etc. The performance of using surrogate model-based optimization, however, highly relies on the accuracy of the surrogate model. Additionally, the design solutions may be in some space where there is no existing sample around. As a result, large amounts of training samples generated from time-consuming simulations are required to build a globally accurate surrogate model, which may cause an acceptable computational time.

To further reduce the number of simulations, the adaptive surrogate model-based optimization strategy, such as Bayesian optimization [17], was developed. Instead of training a perfect surrogate model before optimization, the adaptive strategy builds the initial surrogate model with a small amount of simulations and updates the surrogate model gradually with the optimization processes. In this case, the optimization algorithm is not only used to find the optimal solutions but also used to guide the generation of new samples to update the surrogate models. By efficiently utilizing every simulation to build the surrogate model, the number of simulations used in the entire optimization process can be reduced, which means a shorter computational time. In this paper an adaptive surrogate model-based MOO using LASSO-Artificial Neural Network-Grey Wolf Optimizer (L-ANN-GWO) algorithm [18] has been used in order to determine the optimum welding parameters of a large assembly structure in order to reduce thermal displacement and residual thermal stress.

Consequently, an integrated framework for the prediction and MOO of thermal distortion by coupling FEM with a hybrid L-ANN-GWO approach is developed in this study to realize residual stress and thermal deformation reduction in a heavy machinery component welding. Unlike conventional studies that rely solely on numerical simulations or standalone optimization techniques, the proposed methodology combines physics-based thermal warpage analysis with data-driven intelligence to enhance prediction accuracy and optimization efficiency. To tackle the computational time and accuracy challenges in thermo-elasto-plastic simulation-based optimization, the proposed framework provides a systematic and computationally efficient strategy. The meshes and simulation time steps are well tuned in thermo-elasto-plastic FEM simulation to reduce the simulation time for a single design. The adaptive surrogate model-based optimization algorithm, i.e., L-ANN-GWO, is utilized to reduce the total number of simulation evaluations during the optimization. Additionally, the accuracy of the optimization results is guaranteed by the design verification steps in the adaptive sampling strategy. The proposed framework is applied to an industrial large-scale welding case provided by Ponsse Oyj to reduce the maximum thermal distortion and maximum residual stress by optimizing welding parameters and starting point positions. In this study, we applied optimization to a full industrial heavy machinery assembly rather than laboratory specimens while incorporation of industrial Welding Procedure Specification (pWPS) constraints directly into the optimization problem. The proposed optimized welding parameters are subject to the range of acceptable pWPS provided by Ponsse Oyj. As a result, the optimized cases could reduce maximum plastic displacement by up to 30%. The running time, including all training sample generation and the optimization, is around 10 days with a total of 60 FEM simulations.

The remainder of the paper is organized as follows. In section 2, we have explained all the underlying equations and boundary conditions required for the thermo-elasto-plastic modelling and MOO. In this section we have also explained the case study and welding parameters imposed by pWPS. Results and discussion on the numerical simulation results are presented in section 3. In this section we have also provided 3 optimized cases for welding parameters which results in less thermal stress and distortion. Finally, we conclude this paper in section 4.

2. Material and method

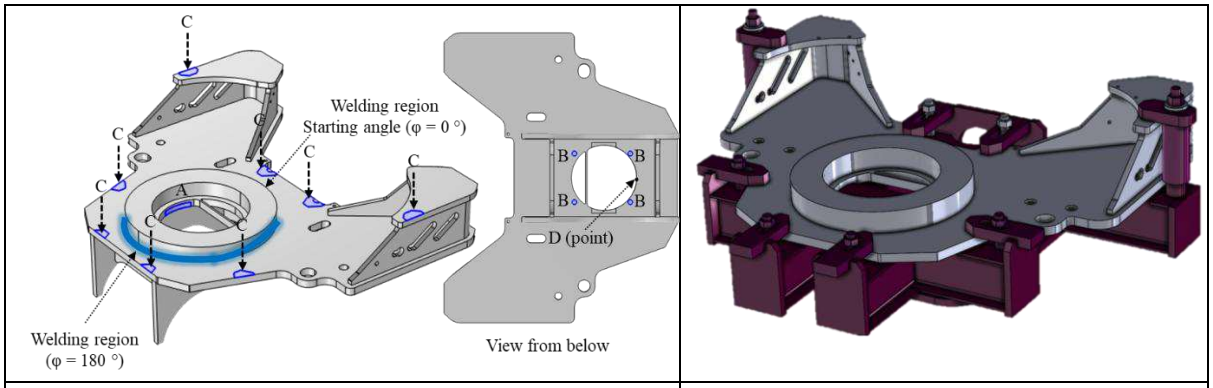
In this study, the front frame assembly of a heavy forestry machine provided by Ponsse Oyj (Fig. 1 (a)) was investigated through thermomechanical analysis using FEM modelling and MOO. During welding, assembly is fixed by special fixtures represented in Fig. 1 (b). The case study geometry is 1.2 m in length, 1 m in width and its height is about 0.5 m. In order to reduce the complexity of thermomechanical model in this study clamps and fixtures are replaced by normal load boundary conditions in mechanical structure analyses. For modelling the release of the structure from the fixture clamps, applies forces are removed after approximately 1200 seconds. This is defined by defining a step function multiplier changing from 1 to 0. To avoid the singularity errors for removing the loads, 3 seconds smoothing was applied to the multiplier step function. Furthermore, to reduce the computation time, unnecessary design details were removed from the intended geometry for FEM analyses.

Two complete circular pulsed Metal Active Gas (MAG) welding (360 °) with Fronius welding machine are carried out to fix the two parts of assembly together. The Preliminary Welding Procedure is represented in Table 1. Based on the pWPS the interpass temperature between two welding must be less 250 °C. Meaning, Welding assembly must be cooled below 250 °C, before starting the second pass of

weld. The objective of the numerical simulation is to determine the displacement and stress induced during welding and provide a reliable model for MOO. The ultimate objective of this study is to find the optimum welding parameters to reduce the induced thermal displacement and thermal stress. Four welding parameters for each circular weld (in total 8) were selected as design space including: starting angle of weld ($\boldsymbol{\varphi}$), voltage ($\boldsymbol{V}$), current ($\boldsymbol{I}$), and travel speed ($\boldsymbol{v}$). Design space of the welding parameters is selected based on the pWPS provided by Ponsse Oyj, represented in Table 1. WFR denotes wire federate and Gf is the gas flow rate. Considering the weld starting angle as a process parameter is one of the key contributions of this study, as this influential welding parameter has been largely neglected in previous studies.

Table 1: Design space of the welding parameters based on the pWPS

	Filler diameter [mm]	**WFR [m.min^{-1}]**	**Gf [l.min^{-1}]**	***V*** **[V]**	***I*** **[A]**	***v*** **[mm.min^{-1}]**	**Heat input [kJ.mm^{-1}]**	***φ*** **[°]**
Pass 1	1.2	16.3 – 16.6	18-22	32.5-33.5	375-395	415-425	1.38 -1.53	0-360
Pass 2	1.2	17.6 – 18.2	18-22	32.5-33.5	420-440	268-275	2.38-2.64	0-360



(a) (b)

Fig. 1: Illustration of the case study; (a) Welding assembly with boundary conditions; (b) welding structure on the fixture during welding

2.1. Creation of numerical simulation

A thermo-elasto-plastic FEM model is created using COMSOL Multiphysics 6.3. Material used for welding assembly is low carbon-grade AH36 steel. To reduce the computation time of FEM, model is simulated with an uncoupled computation model: In the first step of simulation, heat transfer during welding was determined. Obtained results by heat transfer study in the first step have been introduced in the second study which consists of thermomechanical studies.

All thermal and mechanical material properties are defined as temperature-dependent [19,20]. For both welding passes, heat source is modeled by a Goldak double-ellipsoidal heat source model [21]. In the Goldak double-ellipsoidal heat source model, the welding arc is represented by two ellipsoids: a front ellipsoid (ahead of the heat source center), and a rear ellipsoid (behind the heat source center). Parameters of the Goldak heat source equation are represented in Table 3. Goldak equation is applied to the welding region highlighted in Fig. 1 (a). Starting position of the weld for both welding passes are defined as an optimization parameter ($\boldsymbol{\varphi}$). Heat transfer in the model is determined by heat transfer equation represented in equation (1) [22]. The main heat source in this equation is the heat release due to the welding.

$$\rho C_p \cdot \nabla T - \nabla \cdot \boldsymbol{q} = \boldsymbol{Q}_{\mathrm{w}} + Q \qquad (1)$$

Where, $\boldsymbol{q}$ is the heat flux vector due to heat transfer, ρ is density, C_p is temperature dependent-specific heat, $\boldsymbol{Q}_w$ is released heat due to welding, and Q is other heat sources in the system. In this study we assumed that welding heat is the only heat source in the system. Other heat sources such as Joule heating or surface pre-heating are neglected. The heat flux vector ($\boldsymbol{q}$) is related to temperature gradient (∇T) through conduction equation (2), convection equation (3), and thermal radiation (4).

$$\boldsymbol{q} = -K\nabla \mathrm{T} \tag{2}$$

$$\boldsymbol{q} = h(T - T_{env}) \tag{3}$$

$$\boldsymbol{q} = \varepsilon_{em}\sigma_s(T_{env}^4 - T^4) \tag{4}$$

In the thermal radiation equation, ε_{em} is the emissivity coefficient, K is temperature-dependent thermal conductivity, h is the thermal convection equation and σ_s is Stephan-Boltzmann constant. Heat transfer by radiation and free convection are applied to all the surfaces of the structure represented in Fig. 1. In order to compensate for the heat transfer due to the conductivity between welding assembly and fixture under the clamps (regions marked "C" in Fig. 1 (a)), higher convection coefficient (1000 $W.(K.m^2)^{-1}$ is assigned to this region. Heat transfer parameters and boundary conditions used in this study for different locations shown in Fig. 1 (a) are presented in Table 2. Heat source applied during welding is determined using equation (5). Considering the pulsed welding process, the average heat input is reduced according to the duty cycle, resulting in lower net energy deposition compared to continuous welding.

$$\boldsymbol{Q} = \frac{1}{2}.\eta.\boldsymbol{I}.\boldsymbol{V}.f_{Goldak}(x, y, z). \tag{5}$$

Table 2: Heat transfer parameters and applied boundary conditions

Parameter	Value
Surface emissivity coefficient (ε_{em}) [1]	0.8
Free convection coefficient (h) [$W.(K.m^2)^{-1}$]	18
Process efficiency (η)	0.85
Environmental temperature	25 °C
Mechanical boundary condition, Boundary (A)	$u_x = 0$, $u_y = 0$
Mechanical boundary condition, Boundary (B)	$u_z = 0$
Mechanical boundary condition, Boundary (C)	Normal load: $t < 1200$ s → f = 40 [kN] $t \geq 1200$ s → f = 0 [kN]
Mechanical boundary condition, point (D)	$u_x = 0$, $u_y = 0$, $u_z = 0$

Table 3: Parameters of Goldak heat source equation

Parameter	Value
Front Length Parameter (a_f) [mm]	4
Rear Length Parameter (a_r) [mm]	8
Half Width (b) [mm]	3
Depth Parameter (c) [mm]	2
Front Heat Fraction (f_f) [1]	0.6
Rear Heat Fraction (f_r) [1]	1.4

A quasistatic linear elasto-plastic model is developed for modelling the thermomechanical behaviour of the welding assembly during welding. For linear plasticity modelling in COMSOL, the governing equations are usually based on small-strain elastoplastic with: linear elasticity, a yield criterion

(commonly von Mises), flow rule, and hardening law. Temperature-dependent mechanical properties including Young's modulus, Tangent modulus, Yield stress, and thermal expansion coefficient have been implemented for temperature-dependent mechanical modelling. For following thermomechanical modelling, we have assumed than material is isotropic and yield strength is identical in all directions and undergoes made small strain. Furthermore, no kinematic hardening happenings during the process. The equilibrium equation in of mechanical structure represented equation (5) is the fundamental equations in solid mechanics:

$$\Delta \cdot \boldsymbol{\sigma} + \boldsymbol{F}_v = 0 \tag{6}$$

where $\boldsymbol{\sigma}$ is Cauchy stress tensor, and $\boldsymbol{F}_v$ is body force vector. In a linear elastoplastic study, total strain ($\boldsymbol{\varepsilon}$) is decomposed into elastic ($\boldsymbol{\varepsilon}_e$), plastic ($\boldsymbol{\varepsilon}_p$), and thermal strain($\boldsymbol{\varepsilon}_{th}$):

$$\boldsymbol{\varepsilon} = \boldsymbol{\varepsilon}_e + \boldsymbol{\varepsilon}_p + \boldsymbol{\varepsilon}_{th} \tag{7}$$

whereas thermal strain is determined using equation (8):

$$\boldsymbol{\varepsilon}_{th} = \alpha(T)(T - T_{ref}) \tag{8}$$

where *α(T)* is temperature-dependent thermal expansion coefficient. Elastic strain is determined by constitutive Equation (Hooke's Law) represented in (*7*):

$$\boldsymbol{\sigma} = \boldsymbol{C} : \boldsymbol{\varepsilon}_e . \tag{9}$$

where $\boldsymbol{C}$ is the elasticity tensor, $\boldsymbol{\varepsilon}_e$ is the elasticity strain tensor. For the plasticity model we have selected the von Mises yield criterion.

$$f(\boldsymbol{\sigma}, k) = \sigma_{eq} - \sigma_y \tag{10}$$

$$\boldsymbol{\sigma}_{eq} = \sqrt{\frac{3}{2}\boldsymbol{s} : \boldsymbol{s}} \tag{11}$$

Where k is the hardening factor, σ_{eq} is the equivalent von Mises stress, $\boldsymbol{s}$ is deviatoric stress tensor and σ_y is the yield stress. Plastic strain evolution for von Mises plasticity model is determined using equation (9):

$$\dot{\boldsymbol{\varepsilon}}_p = -\lambda \frac{\delta \boldsymbol{F}}{\delta \sigma_y}. \tag{12}$$

Isotropic hardening is a plasticity model that describes how a material becomes stronger as it undergoes plastic deformation. As plastic strain accumulates, the yield stress increases equally in all stress directions. Isotropic hardening model used in plasticity is represented in (12).

$$\sigma_{ys} = \sigma_y + E_{iso}\boldsymbol{\varepsilon}_{pe} \tag{13}$$

$$\frac{1}{E_{iso}} = \frac{1}{E_{Tiso}} + \frac{1}{E} \tag{14}$$

E_{iso} is isotropic hardening modulus and E_{Tiso} is isotropic tangent modulus. Finally, $\boldsymbol{\varepsilon}$ is determined as a function of displacement ($\boldsymbol{u}$) (equation (*14*)).

$$\boldsymbol{\varepsilon} = \frac{1}{2}(\nabla \boldsymbol{u} + (\nabla \boldsymbol{u})^T) \tag{15}$$

Mesh applied to the geometry is illustrated in Fig. 2. A free tetrahedral mesh is applied to the entire geometry. To reduce the computation time and keep the accuracy, separate mesh sizes have been applied to different regions on the structure. However, mesh size in the welding region (represented by blue curve in Fig. 1(a)) have been refined and selected based on times step and welding travel speed. Welding

region's mesh size is approximately 4.2 mm. While for other regions higher mesh sizes is applied. Finally, a mesh convergence study was performed to evaluate the influence of mesh size on the numerical results.

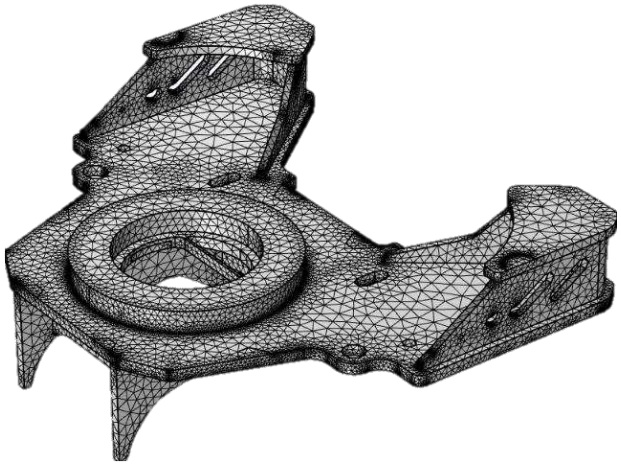


Fig. 2: Applied mesh to the geometry for high fidelity model

In order to reduce the computation time, numerical simulation has been performed in 2 transient study steps. Primary study includes thermal study of welding and secondary study is thermo-mechanical modelling. Results determined by heat transfer study are the inputs for thermo-mechanical study. In order to decrease the computation time during optimization process (low fidelity model), a larger time step is selected, however, for final simulation (high fidelity model), time steps are shortened to increase the accuracy of the results. Different time steps are selected for each study to reduce the computation time while keeping stability. Worth mentioning that it is not possible to apply symmetry boundary condition on FEM model, as φ is one of the optimization parameters and its position effect could not be neglected. Selected time steps during different moments of simulation for both studies are provided in Table 3. In Table 3, short time steps are associate to welding time, while larger time steps are associated to the cooling times and when no welding happenings. To avoid singularity shorter time step is assigned to 10 s of weld 1. Selected time step for cooling after second welding cycle is shorter immediately after welding, due to higher thermal gradient between welding region and environment temperature. While after 1122 s, a larger time step is assigned to decrease the computation time (100 s). To keep the heat transfer stable a strict solver step is selected. MUMPS (MUltifrontal Massively Parallel sparse direct Solver) and PARDISO (PARallel DIrect SOlver) are the solvers used for modelling the heat transfer and thermomechanical modelling respectively.

Table 4: Time steps for different stages of the simulation

	Weld 1		**Interpass cooling**	**Weld 2**	**Cooling**	
Time	0 s -10 s	10 s - 215 s	215 s -265 s	265 s - 622 s	622 s - 1122 s	1122 s - 4500 s
Time step for Heat transfer modelling [s]	0.2	0.4	5	0.4	10	100
Time step for Themo-mechanical modelling [s]	1	1	10	1	10	100

2.2. Multi-objective optimization problem formulation

The overall goal of the study is to minimize distortion and residual stress after the two welding passes. In this case, the maximum displacement ($MaxD$) and the maximum residual stress ($MaxS$) are selected to be the two target parameters that need to be minimized. Note that the maximum displacement position and maximum residual stress position vary when different welding parameters are used. The process parameters for each of the two passes, including $\boldsymbol{V}$, $\boldsymbol{I}$, $\boldsymbol{v}$, and $\boldsymbol{\varphi}$ are the design variables. As shown in Table 1, the ranges of the welding process parameters are defined by pWPS document used in real-world cases, while the starting position can be any point on the welding zone. To make the optimization close to the real case, the process parameters are rounded to one digit, and the starting point are rounded to two digits. In practice, the heat energy input for each welding pass needs to be in a specific range defined in the pWPS document to guarantee the quality of the welds. Thus, the heat inputs are served as the constraints in the MOO. Therefore, the mathematic formulation of the optimization problem can be presented as

$$\begin{aligned} &\text{Find } \boldsymbol{x} = [\boldsymbol{V}_1, \boldsymbol{I}_1, \boldsymbol{v}_1, \boldsymbol{\varphi}_1, \boldsymbol{V}_2, \boldsymbol{I}_2, \boldsymbol{v}_2, \boldsymbol{\varphi}_2]^T \\ &\min \begin{matrix} MaxD(\boldsymbol{x}) \\ MaxS(\boldsymbol{x}) \end{matrix} \\ &\text{s.t. } 1.38 \leq Heat_1(\boldsymbol{x}) \leq 1.53 \\ &\quad 2.38 \leq Heat_2(\boldsymbol{x}) \leq 2.64 \end{aligned} \tag{16}$$

where, the subscripts 1 and 2 represent the first and second pass, respectively. The unit of the heat input is kJ.mm^{-1}. FEM simulation is used to obtain responses of objectives and constraints. Considering the computational costs of one simulation, where it takes five to six hours to run the larger step model, the number of simulations is limited to 60.

2.3. Improved L-ANN-GWO multi-objective optimization algorithm

In this study, the improved L-ANN-GWO algorithm is employed to find the optimal welding process parameters. L-ANN-GWO is a dimension selection-based multi-objective optimization algorithm developed in [18], where the entire design variable set is divided into the group for the objective updating and the group for finding feasible solutions. L stands for LASSO regression used in dimension selection, ANN stands for the artificial neural networks working as the surrogate model to approximate the simulation results, and the GWO represents the gray wolf optimizer which is used to guide the searching in the design space. The main advantage of the algorithm is to reduce the computational time of optimization when time-consuming FEM simulation is used to obtain the objective and constraint responses. Fig. 3 shows the flow chart of the algorithm.

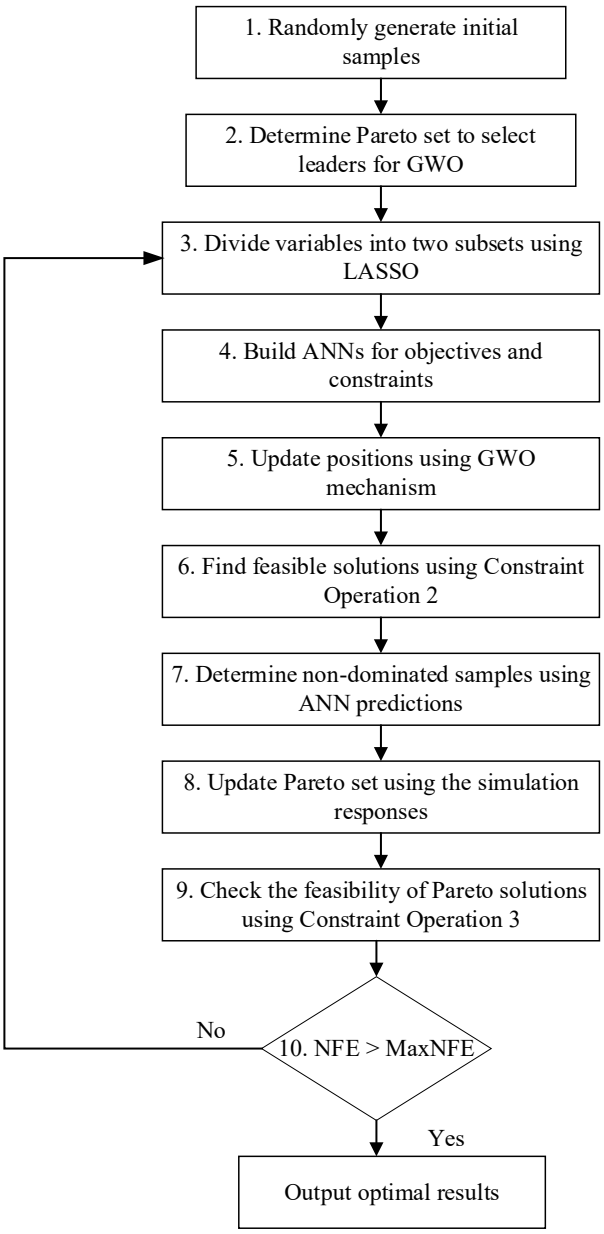


Fig. 3: Flow chart of L-ANN-GWO algorithm [18].

ANNs for each objective and constraints are trained and used to evaluate if a new design generated at the new optimization iteration is better than the existing designs and if the new design is feasible. By replacing the FEM simulation with the surrogate model, the computational time of optimization can be reduced. In this case, a fully connected network with two hidden layers with four hidden neurons in each layer is constructed for each objective and constraint. The adaptive surrogate model training strategy is applied to improve efficiency of optimization by reducing the number of time-consuming simulation evaluations. Different from training an accurate surrogate model by a large amount of training data, the adaptive training strategy builds ANNs starting with a small number of initial samples (20 samples as the default value). At each optimization iteration, new parameter sets are generated via the GWO updating mechanism (block 5 in Fig. 3), and they are evaluated by using the ANNs to select the candidate solutions that are feasible and outperform to the existing solutions (blocks 6 & 7). Then, those candidates are evaluated by the simulation model (block 8) and are judged if they outperform to the existing solutions based on the simulation responses (block 9). Meanwhile, the new evaluated solutions are used to update the ANN models (the feedback loop in the flow chart). Instead of increasing the accuracy of the surrogate model in the entire design space, which may need

large amount of training data, the adaptive training strategy focuses on the more interesting areas and increase the prediction accuracy on those areas. Consequently, by utilizing simulation efficiently, the total optimization time, including simulations, ANNs training, and optimization, can be reduced significantly.

To accelerate the optimization process at the early iterations of the optimization, a LASSO regression-based dimension selection method is applied in L-ANN-GWO to identify the variables that have large impact on the objectives and updating those large impact variables preferentially to increase the convergence speed. Given a linear regression model $\hat{Y} = w_0 + \boldsymbol{X}^T\boldsymbol{w}$, where $\boldsymbol{X}$ represents the position, $\hat{Y}$ is the predicted response from the regression model, and w_0 and $\boldsymbol{w}$ are the coefficients for the linear model, the LASSO regression is to find the value w_0 and $\boldsymbol{w}$ to solve the minimization problem as shown in Eq.(17).

$$\min_{w_0,\boldsymbol{w}} \sum_{i=1}^{n} (Y_i - \hat{Y}_i)^2 + \lambda \sum_{j=1}^{p} |w_j| \tag{17}$$

where n is the number of positions, λ is a non-negative parameter, and p is the number of the coefficients $\boldsymbol{w}$. For a given λ, due to the property of the L_1 regression function (i.e., the second term in Eq. (*17*), some elements in w_0 and $\boldsymbol{w}$ will be zero. By utilizing the parameter shrinking feature of LASSO process, the design variables with non-zero coefficients are identified as the large impact variables which are updated by the GWO updating mechanism shown in Eq. (18).

$$\begin{aligned}
\boldsymbol{x}_{\text{var_obj}}^{new} &= \frac{\boldsymbol{x}_{1,\text{var_obj}} + \boldsymbol{x}_{2,\text{var_obj}} + \boldsymbol{x}_{3,\text{var_obj}}}{3} \\
\boldsymbol{x}_{1,\text{var_obj}} &= \boldsymbol{x}_{\alpha,\text{var_obj}} - A_1 \cdot D_\alpha \\
\boldsymbol{x}_{2,\text{var_obj}} &= \boldsymbol{x}_{\beta,\text{var_obj}} - A_2 \cdot D_\beta \\
\boldsymbol{x}_{3,var_obj} &= \boldsymbol{x}_{\delta,\text{var_obj}} - A_3 \cdot D_\delta \\
D_\alpha &= \left|C_1 \cdot \boldsymbol{x}_{\alpha,\text{var_obj}} - \boldsymbol{x}_{\text{var_obj}}\right| \\
D_\beta &= \left|C_1 \cdot \boldsymbol{x}_{\beta,\text{var_obj}} - \boldsymbol{x}_{\text{var_obj}}\right| \\
D_\delta &= \left|C_3 \cdot \boldsymbol{x}_{\delta,\text{var_obj}} - \boldsymbol{x}_{\text{var_obj}}\right| \\
A_i &= 2ar_{1,i} - a, i = 1,2,3 \\
C_i &= 2 \cdot r_{2,i}, i = 1,2,3 \\
a &= \frac{2(maxNFE - NFE)}{maxNFE}
\end{aligned} \tag{18}$$

where, $\boldsymbol{x}_{\text{var_obj}}$ denotes the high-impact variables, $\boldsymbol{x}_\alpha$, $\boldsymbol{x}_\beta$, and $\boldsymbol{x}_\delta$ represent the three best-performing samples to guide the position updating process, and r_1 and r_2 are random numbers generated in the range [0, 1]. NFE stands for the number of function (i.e., FEM simulation) evaluations, the maximum number of which is used to terminate the optimization process. The details of the GWO updating mechanism can be found in [23].

To further improve the capability of the algorithm to deal with the constrained MOO problems, an improved L-ANN-GWO is developed in this paper. In the original L-ANN-GWO, whether one design is dominated by another is only determined by their objective values. In the improved L-ANN-GWO, the ε-constrained method is added to determine if one design is dominated or dominates the other (i.e., block 2, block 7, and block 8 in Fig. 3). The ε-constrained method follows the criteria:

If $CV(\boldsymbol{x}_1) \leq \varepsilon$, $CV(\boldsymbol{x}_2) \leq \varepsilon$, and $\forall\, f_i(\boldsymbol{x}_1) \leq f_i(\boldsymbol{x}_2)$, $\boldsymbol{x}_1$ dominate $\boldsymbol{x}_2$;

If $CV(\boldsymbol{x}_1) \leq \varepsilon$, and $CV(\boldsymbol{x}_2) > \varepsilon$, $\boldsymbol{x}_1$ dominate $\boldsymbol{x}_2$;

If $CV(\boldsymbol{x}_1) > \varepsilon$, and $CV(\boldsymbol{x}_2) > \varepsilon$, and $CV(\boldsymbol{x}_1) < CV(\boldsymbol{x}_2)$, $\boldsymbol{x}_1$ dominate $\boldsymbol{x}_2$.

ε is the threshold (not mistaken with strain in thermomechanical study), which is selected as 0.1 in this paper. $f_i(\cdot)$ is the response value of the i-th objective. $CV(\cdot)$ is the constraints violation value. In the proposed algorithm, the modified Kreisselmeier and Steinhauser (KS) function is used to calculate the constraint violation value. The expression of KS function used in [24] is employed and shown in Eq. (19).

$$CV(\boldsymbol{x}) = g_{\max}(x) + \frac{1}{\rho}\ln\left[\sum_{j=1}^{nc} e^{\rho\left(g^j_{\text{norm}}(\boldsymbol{x}) - g_{\max}(\boldsymbol{x})\right)}\right] \qquad (19)$$

$$g_{\max}(\boldsymbol{x}) = \max_{j=1\ to\ n}\left(g^j_{\text{norm}}(\boldsymbol{x})\right)$$

Where nc is the number of constraints, ρ is a shape parameter which is set to be 200 in this paper, and $g^j_{norm}(\boldsymbol{x})$ represents the normalized value of j-th constraint response at design $\boldsymbol{x}$, which is formulized as

$$g^j_{norm}(\boldsymbol{x}) = \begin{cases} normalized\ to\ [-1,0], if\ g^j(\boldsymbol{x}) \le 0 \\ normalized\ to\ (0,1], if\ g^j(\boldsymbol{x}) > 0. \end{cases} \qquad (20)$$

3. Results and discussion

3.1. Initial numerical simulation results

Temperature distribution for baseline model at starting point (φ = 0) for both welding cycles is represented in Fig. 4. Based on the pWPS, there is a waiting time between two welding cycles in order to reach below 250°C. Temperature distribution of each region highly depends on the heating cycle and starting position of the welding. As an example, in the case of Fig. 4 (right) four temperature peaks are observed which are related to start and end of the welding. More thermal peaks could lead to more thermal stress in these regions. Consequently, selection of starting points could highly impact the thermomechanical behaviour of the welding structure.

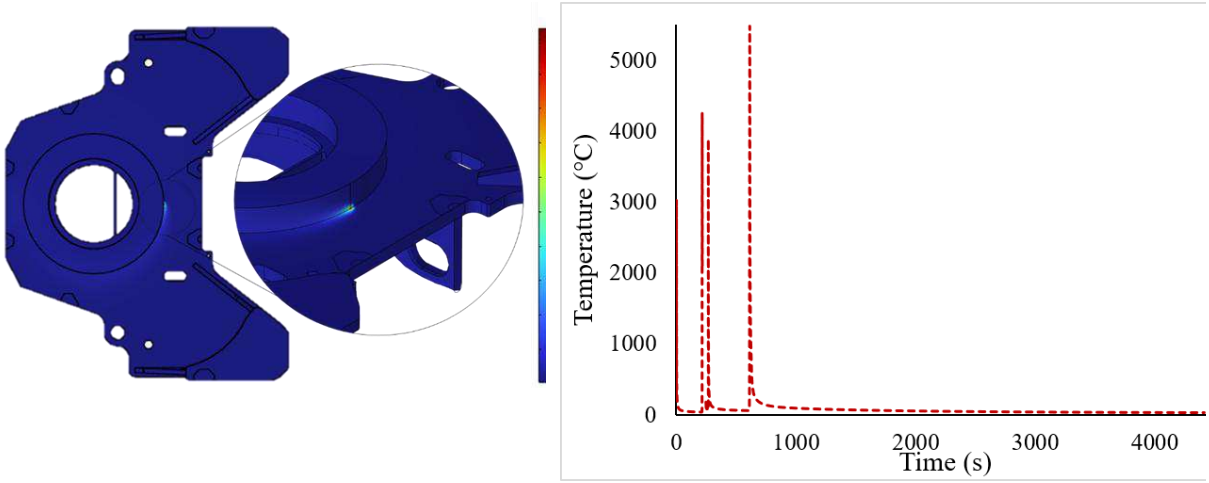


Fig. 4: Temperature distribution of the welding assembly at starting point (φ = 0) at the end of welding stage (t = 622 s) for baseline numerical simulation (left); Temperature distribution according to time for starting point on the structure (right)

Initial displacement and stress due to the applied force by fixture's clamps are presented in Fig. 5. Maximum initial displacement of the welding assembly is approximately 1.75 mm occurring on the sides of the assembly. Displacement is in the same direction of the applied forces presented in Fig. 1 (a). On the other hand, maximum stress is approximately 150 MPa (excluding point D as it is fixed boundary condition), which is around the welding collar. Comparing maximum stress during loading on the clamp with yield stress (σ_y = 300 MPa) at room temperature (25°C) suggests that stress and

displacement presented in Fig. 5 are still in the elastic domain of the steel, meaning that after removing the structure from the fixture, stress and deformation returns to approximately zero value. Equivalent elastic strain (ε_e) for the preloading by clamp is determined by equation (*15*). Consequently, there is no plastic strain in this stage of manufacturing. In this study, we have assumed similar loads from all the clamps to the structure. However, it is dependent on the clamping method such as clamps are applied by operator or it is automatically placed.

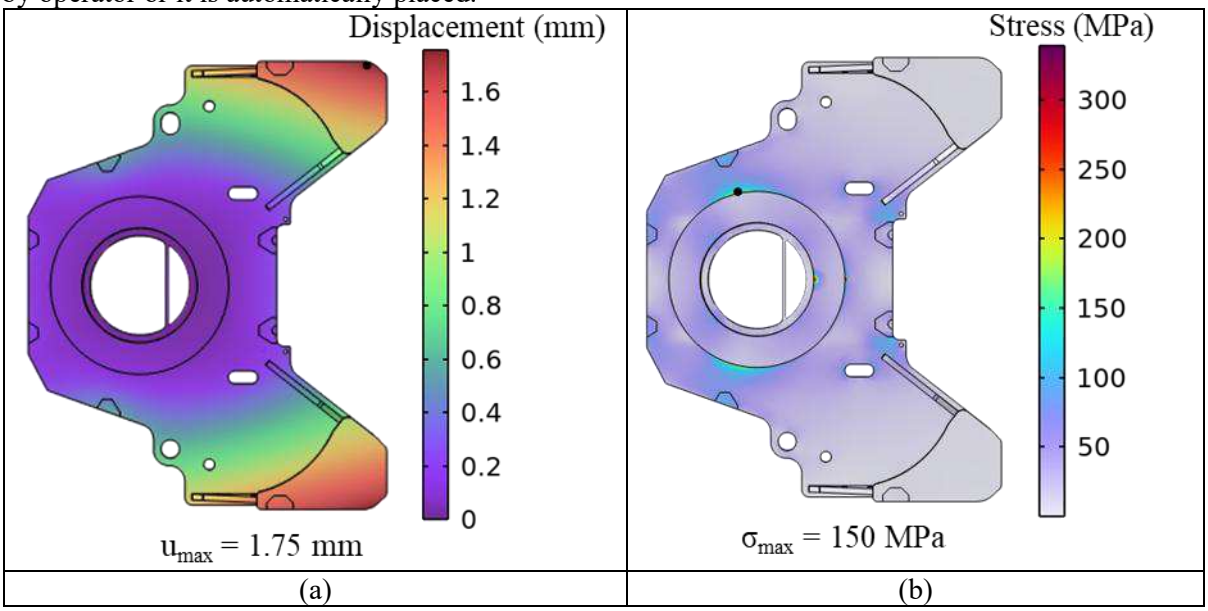


Fig. 5: Initial displacement (a) and stress (b) due to applied forces from the fixture

Depending on the travel speed, first welding cycle ($\boldsymbol{v_1}$ = 420 mm.min^{-1}) ends at about t = 215 s, and second welding cycle ($\boldsymbol{v_1}$ = 430 mm.min^{-1}) ends around t = 620 s After end of second welding cycle until t = 4500 s, structure is cooling until room temperature. At around t = 1300 s when temperature of the structure reaches below 200°C, applied forces for clamps (boundary condition C) are removed from the structure. Thermal displacement during welding and cooling at the maximum point on the assembly is represented in Fig. 7. Four plateaus on the displacement curves are observed. These plateaus on displacement curves correspond to first welding cycle, second welding cycle, assembly cooling under the applied forces by clamps and finally last plateau which is after removing the load applied by clamps. Depending on the selected welding parameters, thermal displacement could reach up to 10 mm. The difference between the third and fourth plateau in displacement curves is approximately equivalent to the elastic displacement $\boldsymbol{u}_e$ represented in Fig 5 (a). As an example, for baseline case $\boldsymbol{u}_e$ is 1.53 mm which is the same value as the difference between third and fourth plateau in its corresponding curve. Contrary to $\boldsymbol{u}_e$, thermal plastic displacement is in z direction. For baseline case, total displacement after first cycle is about 2 mm, while at t = 4500 s residual displacement is 9.88 mm. This suggests that most of the plastic deformation occurs during cooling phase. Our observation on different case studies revealed that maximum displacement position on the structure is dependent on the starting location of second welding cycle. Importance of the second welding pass is mainly due to higher value of $\boldsymbol{I}$ comparing to first welding pass, slower travel speed ($\boldsymbol{v}$) and also accumulated heat due to first welding pass.

Residual stress at t = 4500 s is represented in Fig. 9. Maximum residual stress during welding is observed in the welding region. Location of the maximum stress location is dependent on the starting angle of the second-round welding. As an example, in the case of baseline case, maximum stress is happening on $\boldsymbol{\varphi}$ = 0 °. For baseline case study, after first welding cycle maximum stress is about 6920 MPa, while at t = 4500 s, maximum stress is about 8298 MPa. Contrary to total displacement where the difference between the maximum values after the first cycle and t = 4500 s are noticeable (about 5 times), total maximum stress does not increase significantly during the cooling phase. This suggests that total deformation of the structure highly depends on the cooling rate and is relatively independent from the total heat delivered to the structure during welding. Similar to stress, plastic strain is also happening in the weld zone. Displacement decreases much more than residual stress because distortion

is governed by the overall thermal expansion and contraction of the structure, whereas residual stress is primarily controlled by local plastic deformation and material restraint. Consequently, improving the thermal distribution can substantially reduce deformation while having only a limited effect on the residual stresses, which remain constrained by the material's yielding behaviour.

The numerical simulation results revealed a pronounced concentration of plastic strain within the weld region (plastic strain around 0.9). The elevated plastic deformation observed in these areas can be attributed to the complex thermal cycles and localized stress concentrations generated during the welding process. The weld and localized stress concentrations generated during the welding process. The weld metal experienced higher plastic strain levels compared to the base material due to the combined effects of thermal expansion, contraction, and material softening at elevated temperatures. Furthermore, the steep temperature gradients across the weld joint promoted non-uniform deformation, leading to strain localization near the weld toe and fusion boundaries. As cooling progressed, residual stresses developed and contributed to additional plastic deformation in regions where the local stress exceeded the material yield strength. These highly strained zones are potential sites for crack initiation and fatigue damage under subsequent service loading.

3.2. Multi-objective optimization results

The MOO is operated in the high-performance computing cluster provided by Tampere Center for Scientific Computing. The employed computing node uses 40 cores from two AMD EPYC 7502 32-core processors with 72GB memory. In this condition, the average of one simulation takes around 5.5 hours. 20 initial simulations are evaluated at the beginning of the optimization to train the ANNs and LASSO regression models. The other 40 samples are generated and evaluated gradually during the optimization. When the total number of simulations reaches 60, including the 20 initial simulations, the optimization process terminates and the final optimal results are considered as output. Fig. 6 shows the baseline, all the simulations evaluated during the optimization, and the Pareto front. Note that the baseline is the model where median values of the process parameters listed in Table 1 and the zero degree for both starting points are used.

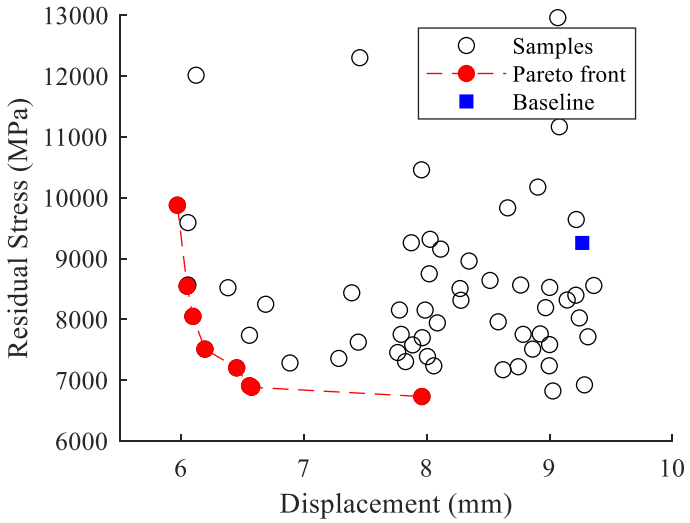


Fig. 6. Residual stress vs. displacement graph performed for optimization

In total, eight Pareto solutions are generated from the optimization. As shown in Fig. 6, compared to the baseline, there are seven solutions which are reduced in both maximum displacement and maximum residual stress, while the rest solution reduced significantly in maximum displacement but increase the maximum residual stress. Table 5 lists the process parameters of three typical solutions, including the one with the minimum displacement (Case 1), the one with the minimum residual stress (Case 3), and the one with balanced displacement and residual stress (Case 2). The maximum displacement, maximum residual stress, maximum plastic strain, and the heat input for each pass for the three selected optimal solutions and the baseline are presented in Table 6, respectively. Note that the simulation called in optimization process is a relatively lower fidelity model with a larger time step to accelerate the

optimization. The selected three solutions are evaluated by a higher fidelity simulation with a precise time step setting. As shown in Table 6, the simulation results of maximum displacement and maximum stress follow the similar trend in low-fidelity model and high-fidelity model. By comparing the optimal solutions with the baseline, the maximum displacement is reduced from 30% to 14% for the selected three solutions while the residual stress reduces 4% in cases 2 and 3 and increases 1% in case one.

Decreased heat input is one of the reasons leading to the reduction of the maximum displacement. Compared to the baseline, the heat input of the first pass remains similar for the three select solutions, especially the third solution has an even higher heat input. The heat input for the second pass reduces more obviously, which leads to a smaller displacement after the cooling stage, as shown in Fig. 7. On the other hand, a higher heat input is benefit to release residual stress as shown in the three optimal solutions. The heat input is controlled by voltage, current, and travel speed together. In case 1, the current and voltage are decreased to reduce the heat input, while the increased travel speed contributes to the lower heat input. In practice, a faster travel speed usually means short welding time, which is more attractive in the real-world industry.

The starting point positions for the two passes are also important, especially in reducing the maximum displacement. The baseline welding uses the same starting points at 0°, which causes accumulated heat and transfer to the same edge of the part. As shown in Fig. 7, the maximum displacement of the baseline is not the largest after the first pass, but it increases much more than other three solutions after the second pass with the same starting point. By arranging the starting points for the two welding passes in different positions, the displacement caused by thermal can be well distributed. As shown in Fig. 8, the distribution of the displacement in case 1 and case 2 are almost symmetric, and both two cases are also smaller in maximum displacement compared to the other two welding cases. The separate pass 1 and pass 2 starting points re-distributed the temperature field and reduced the differences between the left and right of the welding part, leading to a reduced maximum displacement. Additionally, since more heat is input during the second pass, putting the starting point for the second pass far away from the bottom (i.e., 0°) can reduce the temperature gradient from the end welding point to the bottom left or bottom right edge of the part. The smaller temperature gradient leads to a smaller thermal-plastic displacement after cooling down.

In summary, smaller heat input, separate starting points, and ranging the starting points far away from the bottom can reduce the displacement while a higher heat input can reduce the residual stress. To balance both objectives, the solution of case 2 is the most attractive solution, which reduces maximum displacement by 25.8% and reduces the maximum residual stress by 4.2%.

Table 5: Value of optimized process parameters for each welding pass

	V_1 [V]	I_1 [A]	v_1 [mm.min^{-1}]	φ_1 [°]	V_2 [V]	I_2 [A]	v_2 [mm.min^{-1}]	φ_2 [°]
Minimum thermal displacement (Case 1)	32.5	375	415	77.42	32.5	420	268	157.19
Balanced displacement and residual stress (Case 2)	33.3	375	422.7	322	33.1	427	270	90
Minimum residual stress (Case 3)	33.2	392.5	424.8	180	32.6	427.3	271.1	340
Baseline	33	385	420	0	33	430	261	0

Table 6: Value of mechanical responses for different optimized cases compared to baseline

		Case 1	**Case 2**	**Case 3**	**Baseline**
Displacement [mm]	Low fidelity	5.968	6.556	7.960	9.267
	High fidelity	6.878	7.355	8.491	9.884
Stress [MPa]	Low fidelity	9878	6901	6732	9257
	High fidelity	8392	7952	7815	8298
Plastic strain [1]	Low fidelity	0.9642	0.9590	0.8516	0.8549
	High fidelity	0.9365	1.288	1.02	0.9089

Heat input [kJ.mm^{-1}]	Pass 1	1.41	1.42	1.47	1.45
	Pass 2	2.44	2.51	2.47	2.61

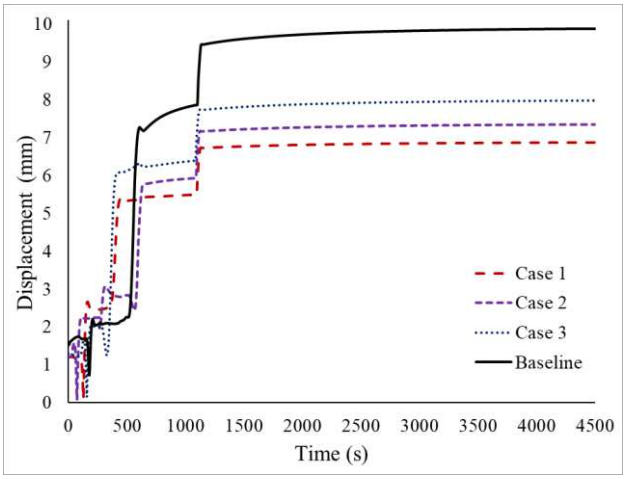


Fig. 7: Thermal displacement based on different welding parameters for maximum point on the assembly

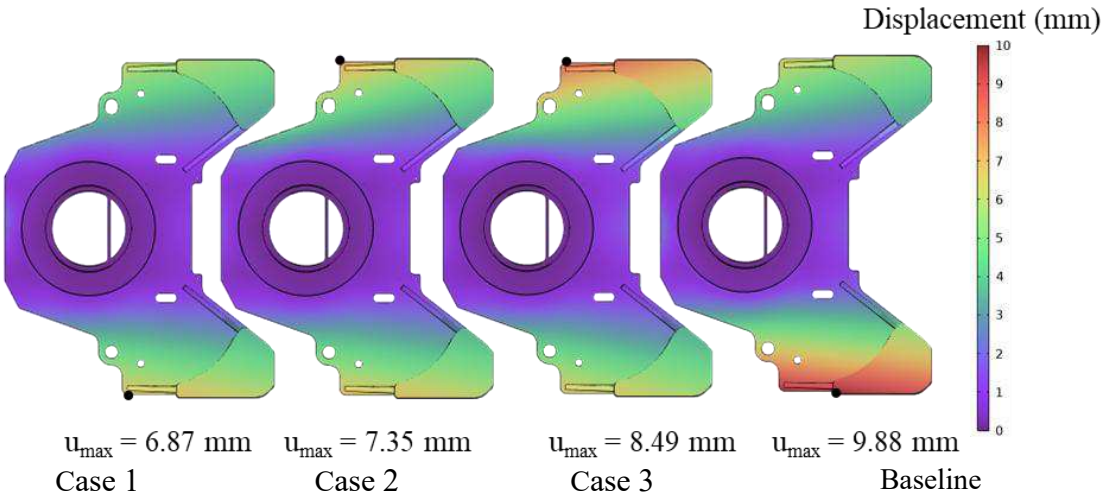


Fig. 8: Comparison between displacement values determined for different case studies

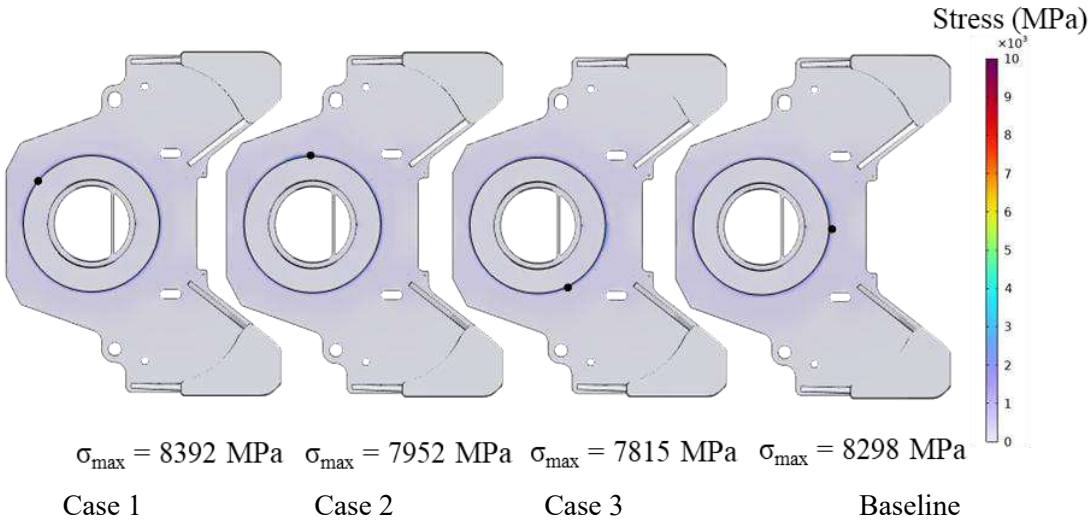


Fig. 9: Comparison between von Mises stress values determined for different case studies

4. Conclusion

In this paper, a thermo-elasto-plastic numerical model for modelling thermal deformation and stress of a large machinery structure under pulsed Fronius welding has been developed using Finite element modelling. Furthermore, a MOO by L-ANN-GWO algorithm approach is applied to find optimum welding parameters such as starting point, current, travel speed and voltage for thermal deformation and stress reduction. The numerical simulation and optimization algorithm presented in this paper were specifically designed to address the limitations arising from the computationally demanding numerical model and the need to perform a large number of model evaluations during the optimization process. Selected algorithm in this study, is able to find optimum process parameters with least running full numerical thermomechanical model. The objective of optimization is to reduce thermal stress and thermal deformation while keeping the design space of the parameters in an acceptable range based on the Preliminary Welding Procedure Specification (pWPS).

Our studies revealed the importance of welding starting position on thermal distortion and stress. Selection of optimized welding starting position is a practical contribution for industrial welding planning and could be included in the pWPS. Furthermore, our studies revealed that total deformation is highly dependent on the cooling rate of the structure. In this study, we have proposed three process parameters combinations which result in smaller design objectives. Optimized combinations could reduce the displacement to 40% of induced deformation during welding process. In this study, we have considered constant load from the clamps on the welding structure. For future studies, we will investigate the effect of load applied by clamps on the thermal deformation and performing MOO on the applied loads. Applying adjusted load could further decrease the thermal deformation due to welding. Considering the size of the structure, performing experimental study is very challenging on this case study. Experimental validation of numerical validation and comparison between the cases experimentally are future studies.

Acknowledgement

The authors also want to thank Ponsse Oyj company for providing the case study and its related documentation and technical support and thank Tampere Center for Scientific Computing for providing computational resources. For this paper, a Large Language Model (LLM) was used to assist with rephrasing and improving the quality of the text. The authors take full responsibility for the content of this paper and for the use of artificial intelligence (AI) in its preparation.

Declaration

a. **Funding:** This work is supported by Business Finland "Robot box project" with project number 312204464911.

b. **Conflicts of interest:** The authors declare that they have no conflicts of interest.

References

[1] Y.M. Zhang, Y.-P. Yang, W. Zhang, S.-J. Na, Advanced Welding Manufacturing: A Brief Analysis and Review of Challenges and Solutions, Journal of Manufacturing Science and Engineering 142 (2020) 110816. https://doi.org/10.1115/1.4047947.

[2] American Welding Society, Y.-P. Yang, Recent Advances in the Prediction of Weld Residual Stress and Distortion - Part 1, WJ 100 (2021) 151–170. https://doi.org/10.29391/2021.100.013.

[3] D. Deng, H. Murakawa, W. Liang, Numerical simulation of welding distortion in large structures, Computer Methods in Applied Mechanics and Engineering 196 (2007) 4613–4627. https://doi.org/10.1016/j.cma.2007.05.023.

[4] H. Long, D. Gery, A. Carlier, P.G. Maropoulos, Prediction of welding distortion in butt joint of thin plates, Materials & Design 30 (2009) 4126–4135. https://doi.org/10.1016/j.matdes.2009.05.004.

[5] American Welding Society, Y.-P. Yang, Recent Advances in the Prediction of Weld Residual Stress and Distortion - Part 2, WJ 100 (2021) 193–205. https://doi.org/10.29391/2021.100.016.

[6] M. Adak, N.R. Mandal, Numerical and experimental study of mitigation of welding distortion, Applied Mathematical Modelling 34 (2010) 146–158. https://doi.org/10.1016/j.apm.2009.03.035.

[7] J. Souto, E. Ares, P. Alegre, Procedure in Reduction of Distortion in Welding Process by High Temperature Thermal Transient Tensioning, Procedia Engineering 132 (2015) 732–739. https://doi.org/10.1016/j.proeng.2015.12.554.

[8] D.A. Price, S.W. Williams, A. Wescott, C.J.C. Harrison, A. Rezai, A. Steuwer, M. Peel, P. Staron, M. Koçak, Distortion control in welding by mechanical tensioning, Science and Technology of Welding and Joining 12 (2007) 620–633. https://doi.org/10.1179/174329307X213864.

[9] S. Karumuri, B. Haldar, A. Pradeep, S.A.K. Karanam, M.N.S. Sri, P. Anusha, N. Sateesh, R. Subbiah, S. Vijayakumar, Multi-objective optimization using Taguchi based grey relational analysis in friction stir welding for dissimilar aluminium alloy, Int J Interact Des Manuf 18 (2024) 1627–1644. https://doi.org/10.1007/s12008-023-01529-9.

[10] N. Ansaripour, A. Heidari, S.A. Eftekhari, Multi-objective optimization of residual stresses and distortion in submerged arc welding process using Genetic Algorithm and Harmony Search, Proceedings of the Institution of Mechanical Engineers, Part C: Journal of Mechanical Engineering Science 234 (2020) 862–871. https://doi.org/10.1177/0954406219885977.

[11] Y. Li, M. Xiong, Y. He, J. Xiong, X. Tian, P. Mativenga, Multi-objective optimization of laser welding process parameters: The trade-offs between energy consumption and welding quality, Optics & Laser Technology 149 (2022) 107861. https://doi.org/10.1016/j.optlastec.2022.107861.

[12] B. Yi, X. Zhou, C. Shen, J. Wang, Computational investigation on transient thermal tensioning for mitigation of welding induced buckling by elastic FE method, Journal of Manufacturing Processes 83 (2022) 590–606. https://doi.org/10.1016/j.jmapro.2022.09.035.

[13] Y. Tan, G. Zhu, F. Tian, Z. Zhao, B. Chai, Multi-objective optimization of T-shaped bilateral laser welding parameters based on NSGA-II and MOPSO, J Mater Sci 59 (2024) 9547–9573. https://doi.org/10.1007/s10853-024-09727-w.

[14] I. Sabry, M. ElWakil, Hybrid FEM–ML framework for multi-objective optimization of mechanical properties and surface quality in dissimilar AA6061-T6/AA6082-T6 friction stir welding, Materials Today Communications 52 (2026) 115197. https://doi.org/10.1016/j.mtcomm.2026.115197.

[15] P. Sevvel, J. Gunasekaran, J.V. Roy, A. Sivaramakrishnan, V. Choudri, M.A. Murugan, Multi-Objective Optimization of Parameters during Friction Stir Welding of AM50A Mg Alloy Using Genetic Algorithm and Desirability Function Approach for Maximizing Tensile Strength and

Hardness, J. of Materi Eng and Perform 35 (2026) 976–995. https://doi.org/10.1007/s11665-025-11516-8.
[16] X. Zhang, Y. Guo, X. Fan, J. Zhao, B. Yan, L. Zhang, Multi-objective optimization of laser welding process parameters of steel/Al based on BO-RF and MOJS, J Mech Sci Technol 38 (2024) 861–871. https://doi.org/10.1007/s12206-024-0133-x.
[17] H. Deng, P. Gao, H. Xiong, X. Gao, Experiments on resistance spot welding of three layers of unequal thickness steel based on deep learning and multi-objective optimization, CIRP Journal of Manufacturing Science and Technology 61 (2025) 497–512. https://doi.org/10.1016/j.cirpj.2025.07.005.
[18] D. Wu, D. Sotnikov, G. Gary Wang, E. Coatanea, M. Lyly, T. Salmi, A Dimension Selection-Based Constrained Multi-Objective Optimization Algorithm Using a Combination of Artificial Intelligence Methods, Journal of Mechanical Design 145 (2023). https://doi.org/10.1115/1.4062548.
[19] D. Kang, L. Dai, K.-B. Park, Y.-H. Choi, J.-H. Kim, S.-K. Kim, J.-M. Lee, Experimental and Numerical Predictions of Cryogenic Leakages in Welded Steel Plates, Applied Sciences 13 (2023) 3132. https://doi.org/10.3390/app13053132.
[20] E.J.G. Nascimento, E. Dos Santos Magalhães, L.E. Dos Santos Paes, A literature review in heat source thermal modeling applied to welding and similar processes, Int J Adv Manuf Technol 126 (2023) 2917–2957. https://doi.org/10.1007/s00170-023-11253-z.
[21] G. Fu, J. Gu, M.I. Lourenco, M. Duan, S.F. Estefen, Parameter determination of double-ellipsoidal heat source model and its application in the multi-pass welding process, Ships and Offshore Structures 10 (2015) 204–217. https://doi.org/10.1080/17445302.2014.937059.
[22] COMSOL Multiphysics, HeatTransferModuleUsersGuide, (n.d.). https://doc.comsol.com/5.3a/doc/com.comsol.help.heat/HeatTransferModuleUsersGuide.pdf.
[23] S. Mirjalili, S. Saremi, S.M. Mirjalili, L. dos S. Coelho, Multi-objective grey wolf optimizer: A novel algorithm for multi-criterion optimization, Expert Systems with Applications 47 (2016) 106–119. https://doi.org/10.1016/j.eswa.2015.10.039.
[24] G.H. Cheng, G. Gary Wang, Y.-M. Hwang, Multi-Objective Optimization for High-Dimensional Expensively Constrained Black-Box Problems, Journal of Mechanical Design 143 (2021). https://doi.org/10.1115/1.4050749.